

Measurement of the $7p\ ^2P_{3/2}^o$ State Branching Fractions in Ra^+

M. Fan,^{1,2} C. A. Holliman,^{1,2} S. G. Porsev,^{3,4} M. S. Safronova,^{3,5} and A. M. Jayich^{1,2,*}

¹*Department of Physics, University of California, Santa Barbara, California 93106, USA*

²*California Institute for Quantum Entanglement, Santa Barbara, California 93106, USA*

³*Department of Physics and Astronomy, University of Delaware, Newark, Delaware 19716, USA*

⁴*Petersburg Nuclear Physics Institute of NRC “Kurchatov Institute”, Gatchina, Leningrad District, 188300, Russia*

⁵*Joint Quantum Institute, National Institute of Standards and Technology*

and the University of Maryland, College Park, Maryland 20742, USA

(Dated: May 12, 2022)

We report the first measurement of the radium ion’s $7p\ ^2P_{3/2}^o$ state branching fractions and improved theoretical calculations. With a single laser-cooled radium-226 ion we measure the $P_{3/2}$ branching fractions to the $7s\ ^2S_{1/2}$ ground state 0.876 78(20), the $6d\ ^2D_{5/2}$ state 0.107 59(10), and the $6d\ ^2D_{3/2}$ state 0.015 63(21).

I. INTRODUCTION

Precise values for electric dipole matrix elements (MEs) provide fundamental knowledge of atomic and molecular systems and are needed for many applications, including studies of fundamental symmetries and development of atomic clocks. Precision measurements are vital for development of high precision theory, in particular for heavy systems. For example, in an atomic parity non-conservation (PNC) experiment precise information about the atom’s electronic structure is critical to compare the experimental result with the prediction of the standard model. A single radium ion has been considered for PNC measurements due to both its large nuclear charge ($Z = 88$), as PNC effects scale as Z^3 , and the high degree of control available in the system [1–3].

For an electronic state connected to multiple lower-lying states through dipole allowed transitions an extraction of MEs from the lifetime measurements requires measuring the corresponding branching fractions. Here we report the first measurement of the radium ion’s $7p\ ^2P_{3/2}^o$ branching fractions to the ground $7s\ ^2S_{1/2}$ state and the long-lived $6d\ ^2D_{3/2}$ and $6d\ ^2D_{5/2}$ states.

The $E1$ transition amplitudes were calculated earlier for a number of the low-lying states, using different methods [4–6]. In particular, in Ref. [4] the linearized coupled-cluster single double (LCCSD) approach was applied. This is a very effective method but its accuracy is limited because certain smaller corrections due to, for example, non-linear terms and triple excitations are not taken into account. In this work, we include valence triples excitations (solving the equations for triple cluster amplitudes iteratively) and non-linear terms in the framework of the coupled-cluster approach. Based on Cs high-precision studies [7] we can expect strong cancellation of these contributions, but very few experimental results are of sufficient accuracy to allow a comprehensive assessment of these effects, and of these measurements most are in

lighter systems. This work provides needed benchmarks to gauge the importance of these effects for heavy atoms.

Moreover, using very precise measurement of the $P_{3/2}$ to $D_{5/2}$ branching fraction and an accurate calculation of the ratio of the $P_{3/2}$ to $D_{5/2}$ and $P_{3/2}$ to $D_{3/2}$ branching fractions, we are able to extract the value of the $P_{3/2}$ to $D_{3/2}$ branching fraction, reducing its uncertainty by a factor of two compared to the pure experimental result.

The theory-experimental comparison carried out here also provides important information for predicting properties of superheavy elements with $Z > 100$ where precision theory is needed for prediction of energies and matrix elements prior to difficult one-atom-at-a-time spectroscopy studies [8]. Precision theory predictions allow for quick transition searches, which are particularly important due to limited beam time.

II. EXPERIMENTAL SETUP

We measure the branching fractions of the $P_{3/2}$ state to the $S_{1/2}$ (r), $D_{5/2}$ (s), and $D_{3/2}$ (t) states using a single laser-cooled radium-226 ion in a linear Paul trap. The relevant energy levels and laser wavelengths are shown in Fig. 1. The experimental setup is described in [9]. In this work the rf trapping frequency is 1.8 MHz and a static magnetic field of about 3 Gauss is applied along the trap’s axial direction. Similar precision measurements of branching fractions from the $P_{3/2}$ state have been done in Ca^+ [10], Sr^+ [11], and Ba^+ [12].

All laser frequencies and amplitudes for cooling and optical pumping are controlled with double passed acousto-optic modulators (AOMs). We program pulse sequences to a field-programmable gate array (FPGA) that controls the AOMs [13]. Because the $P_{3/2}$ state decays to three states we use two pulse sequences, r - s see Fig. 2 a) and r - t see Fig. 2 b), to measure the three branching fractions. In both sequences we perform state detection where 468 nm light is collected on a photomultiplier tube (PMT) while the $S_{1/2} - P_{1/2}$ and $D_{3/2} - P_{1/2}$ transitions are driven at 468 nm and 1079 nm respectively. If the ion fluoresces, the population was in the $S_{1/2}$ or $D_{3/2}$

* jayich@gmail.com

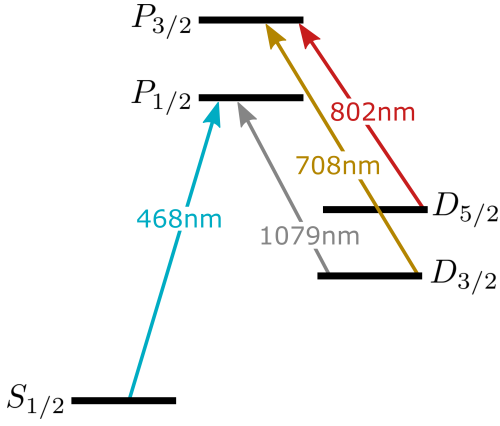


FIG. 1. The laser wavelengths and radium ion energy levels used to measure the $P_{3/2}$ branching fractions.

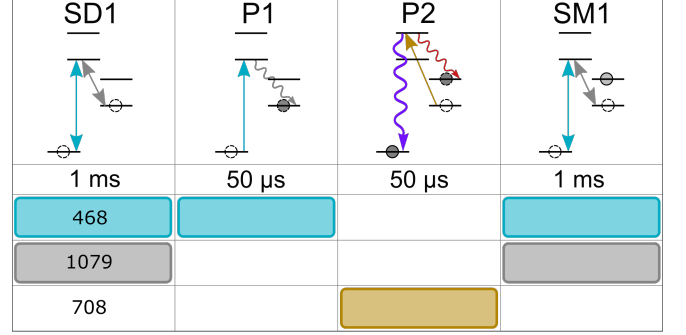
states. If dark, the ion was either shelved in the $D_{5/2}$ state or has left the imaging region. We also perform state measurements, where again 468 nm and 1079 nm light is used, but the collected light is analyzed with a different technique. Both the r - s and r - t pulse sequences begin with 1 ms of state detection. At the end of both pulse sequences we optically pump at 802 nm for 50 μ s to remove population from the $D_{5/2}$ state, and then laser cool for 200 μ s.

The r - s pulse sequence, Fig. 2 a), measures the ratio of the $P_{3/2}$ branching fractions to the $S_{1/2}$ and $D_{5/2}$ states. After the initial state detection (SD1) the population is optically pumped for 50 μ s to the $D_{3/2}$ state with 468 nm light (P1). The population is then pumped at 708 nm for 50 μ s through the short-lived $P_{3/2}$ state to the $S_{1/2}$ and $D_{5/2}$ states (P2). Then one 1 ms of state measurement (SM1) determines whether the ion is in the $S_{1/2}$ or the $D_{5/2}$ state. The measured $D_{5/2}$ population fraction of SM1, p_{rs} , is related to the branching fractions r and s by $p_{rs} = s/(r + s)$.

The r - t pulse sequence, Fig. 2 b), does not measure a simple quantity, such as a branching fraction ratio, but when combined with the r - s result we can determine all of the $P_{3/2}$ branching fractions. After the initial state detection the ion is optically pumped to the $D_{5/2}$ state using 200 μ s of 468 nm and 708 nm light (P1). We state detect for 1 ms to verify pumping to the $D_{5/2}$ state (SD2). Population that might have entered the $D_{3/2}$ state during SD2 is optically pumped to the ground state with 50 μ s 1079 nm pulse (P2). The $D_{5/2}$ population is then optically pumped (P3) with 802 nm light (50 μ s) through the $P_{3/2}$ state to populate the $S_{1/2}$ and $D_{3/2}$ states. The $D_{3/2}$ population is then pumped at 708 nm (50 μ s, P4) through the $P_{3/2}$ state where decays increases the ground state and the $D_{5/2}$ state populations. The $D_{5/2}$ state population fraction, p_{rt} , is measured with a final state measurement (1 ms, SM1). The relationship between the measured $D_{5/2}$ state population fraction, p_{rt} , and the branching fractions is $p_{rt} = p_{rs} \times t/(r + t)$.

We use two methods to determine the ion's electronic

a) r - s pulse sequence



b) r - t pulse sequence

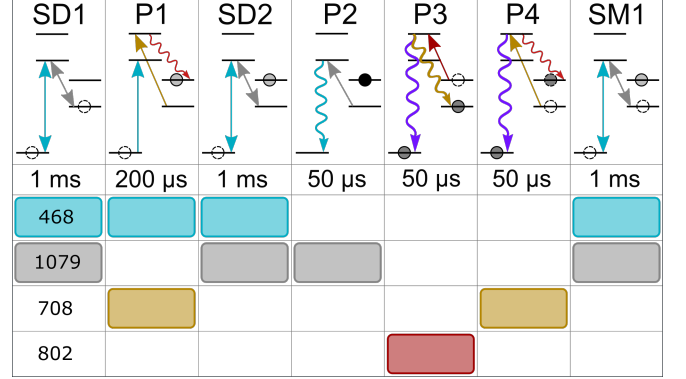


FIG. 2. The r - s and r - t pulse sequences for measuring the radium ion's $P_{3/2}$ state branching fractions. The abbreviated energy level structure is shown in detail in Fig. 1. Each sequence is preceded by 50 μ s of 802 nm cleanout from the $D_{5/2}$ state and 200 μ s of Doppler cooling. The r - s sequence is repeated 11 360 000 times, and the r - t sequence is repeated 3 050 000 times.

state: state detection and state measurement. The state detection method is used to post select data where population is correctly initialized. The state measurement method is used to analyze the final population in the $D_{5/2}$ state. Population initially in the $D_{5/2}$ dark state may be mislabelled as bright state population because the ion can spontaneously decay from the $D_{5/2}$ state during state detection. This effect is accounted for with the state measurement method.

During 1 ms of state detection, if the ion was in the $S_{1/2}$ or $D_{3/2}$ states we count on average 35 photons with a PMT, whereas if the population was in the $D_{5/2}$ state, there are only 1 count on average. We set a state detection threshold at 10.5 counts, which detects bright events with greater than 99.997% efficiency from Poisson statistics. However, due to the $D_{5/2}$ state decays, 0.2% of dark events are mislabelled as bright events with the state detection method.

The state measurement method uses a maximum likelihood technique that analyzes the PMT counts from all pulse sequence measurements to calculate the $D_{5/2}$ state population [10]. We model the bright state counts as a Poisson distribution. The dark state counts are modeled

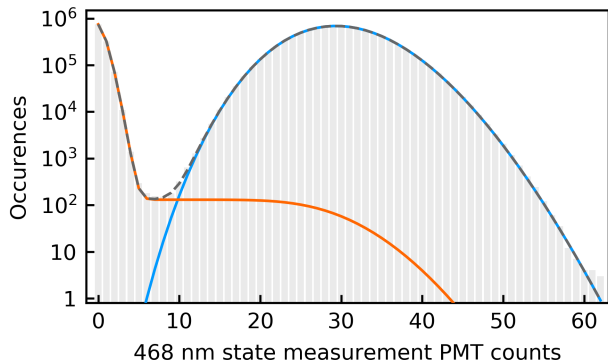


FIG. 3. A histogram of 468 nm PMT counts during state measurement 1 (SM1) of the r - s sequence. The x -axis is PMT counts in 1 ms state measurements, and the y -axis is the occurrences of each PMT count. The maximum likelihood calculation for the dark state probability yields $p_{rs} = 0.10928(10)$ for the r - s sequence. The orange curve is the PMT counts distribution of dark events, and the blue curve is the PMT counts distribution for bright events. The gray dashed curve is the PMT counts distribution for all events, the sum of dark and bright.

as a weighted sum of Poisson distributions where the average dark state counts increase if the $D_{5/2}$ state decays closer to the start of the 1 ms state measurement pulse, see Fig. 2 a), b) SM1. We use the theoretical lifetime 303(4) ms from [4] to calculate the dark state Poisson distribution weights. The dark events occur with probability p_d (bright events occur with probability $p_b = 1 - p_d$). The dark state probability p_d that maximizes the probability that the experimentally collected counts are observed, see Fig. 3, is the maximum likelihood value of p_d . The uncertainty of p_d is $\Delta p_d = \sqrt{p_d(1 - p_d)/M}$, where M is the number of state measurements. For more information on the state measurement PMT counts model and the maximum likelihood technique see Appendix A.

III. EXPERIMENTAL RESULTS

We condition the data from both pulse sequences based on the state detection results. For the r - s sequence if the first state detection after Doppler cooling is dark, we reject the data point as the ion was either not in the imaging region, or the ion was shelved in the long-lived $D_{5/2}$ state. From 11 360 000 events 753 482 were rejected, where the majority of rejected events were excluded due to the electron population being shelved in the $D_{5/2}$ state at the start of the sequence. The rejected events stem from the fact that 802 nm light is not used during the r - s sequence, and therefore is not kept on resonance so occasionally the 802 nm reset pulse at the end of each sequence may fail.

Similarly, for the r - t sequence we discard the data point if the first state detection is dark (962 rejected out of

3 050 000). 802 nm light is kept on resonance with $\text{Ra}^+ D_{5/2} - P_{3/2}$ transition for the r - t sequence, which results in fewer rejected SD1 data points compared to the r - s sequence. We count consecutive rejected data points as a single collision or motional heating event, and the rejected data corresponds to 19 collision or heating events, yielding a collision or heating rate of 0.0018 Hz, agreeing with the measured collision and motional heating rate of 0.0017(4) Hz (See Appendix B). If the second state detection is bright, we also discard the data point, as it indicates that the P1 pumping step failed, or the ion decayed from the $D_{5/2}$ state. Of 3 049 038 events 8049 were rejected, which agrees with the decay probability from the $D_{5/2}$ state during state detection given the $D_{5/2}$ lifetime and $D_{5/2}$ deshelling rate due to 802 nm AOM leakthrough (Appendix C).

With the equations for p_{rs} and p_{rt} , we can calculate the branching fractions

$$r = \frac{(1 - p_{rs})(p_{rs} - p_{rt})}{p_{rs}(1 - p_{rt})} \quad (1)$$

$$s = \frac{p_{rs} - p_{rt}}{1 - p_{rt}} \quad (2)$$

$$t = 1 - r - s \quad (3)$$

We have 10 606 518 data points for the r - s sequence, and the maximum likelihood value for the dark event probability is $p_{rs} = 0.10928(10)$. We have 3 040 989 data points for the r - t sequence, and the maximum likelihood value for the dark event probability is $p_{rt} = 0.00192(3)$. Using Eqs. 1-3, we calculate the statistical branching fractions: $r_{\text{stat}} = 0.87677(20)$, $s_{\text{stat}} = 0.10757(10)$, and $t_{\text{stat}} = 0.01565(21)$.

IV. SYSTEMATIC EFFECTS

The systematic uncertainties and shifts that affect the branching fractions along with the statistical results are summarized in Table I. The systematics are discussed below with further details in the Appendices B-D.

There is a systematic uncertainty due to the combination of collisions and motional heating. Inelastic collisions can change the ion's electronic state. Elastic collisions or motional heating from trap electrode noise can Doppler shift the ion's transitions or bump the ion out of the imaging region, reducing the number of scattered photons and leading to a false dark detection event when the ion is in a bright state. Both collisions and motional heating shift the state measurement probabilities. We measure a total collision and heating rate of 0.0017(4) Hz for a single radium ion in the trap (Appendix B). We assume a maximum collision rate of 0.0021 Hz to calculate shifts for the state measurement probability. Because we do not know the direction of the shift, we assign systematic uncertainties to the branching fractions, See Table I.

TABLE I. Shifts and uncertainties for the $P_{3/2}$ branching measurement.

Source	r	s	t
Statistical	0.87677(20)	0.10757(10)	0.01565(21)
Collisions & Motional Heating	$0(4) \times 10^{-5}$	$0(1) \times 10^{-5}$	$0(4) \times 10^{-5}$
802 nm AOM Leak SM	$-3(1) \times 10^{-5}$	$3(1) \times 10^{-5}$	$0(3) \times 10^{-6}$
State Detection Fidelity	$1.5(4) \times 10^{-5}$	$2(1) \times 10^{-6}$	$-1.6(4) \times 10^{-5}$
Finite $D_{5/2}$ and $D_{3/2}$ Lifetimes	$1.48(2) \times 10^{-5}$	$-1.12(2) \times 10^{-5}$	$-3.6(1) \times 10^{-6}$
AOM Leak State Preparation	$3(1) \times 10^{-6}$	$-2(1) \times 10^{-6}$	$-1(7) \times 10^{-7}$
Total	0.87678(20)	0.10759(10)	0.01563(21)

We calculate the systematic shifts and uncertainties during state preparation due to the finite pumping time, decays from the $D_{3/2}$ and the $D_{5/2}$ states, and finite AOM extinction ratios by modeling the population evolution during state preparation for both the r - s and r - t sequences. The measured $1/e$ pumping time for each state preparation step is $\leq 1 \mu\text{s}$, which is much shorter than the state preparation pulses that are $\geq 50 \mu\text{s}$. Therefore, the finite pumping time shifts the final branching fraction results by less than 1×10^{-9} , which is negligible compared to the statistical uncertainties, and therefore not included in Table I.

The finite state detection fidelity of the SD2 in r - t sequence and SD1 in r - s sequence, due to Poisson statistics and the $D_{5/2}$ state decays, shifts the measured branching fractions. We calculate the shifts using the $D_{5/2}$ and $D_{3/2}$ state lifetimes and the $D_{5/2}$ branching fractions from Pal, *et al.* [4]. In the r - t pulse sequence we use pumping step P2 to pump $D_{3/2}$ state population that has decayed from the $D_{5/2}$ state during SD2 to the $S_{1/2}$ state. Without P2, the pumping step P4 transfers residual population in the $D_{3/2}$ state to the $D_{5/2}$ state, and introduces a systematic uncertainty on the order of 1% for t .

AOM light leakthrough could pump population to undesired states during state preparation. We measure the desheling rates due to AOM leakthrough (See Appendix C), and calculate the systematic shifts and uncertainties due to AOM light leakthrough, which are included in Table I.

802 nm AOM leakthrough during state measurements shifts the $D_{5/2}$ state probability calculated using the maximum likelihood method, as 802 nm leakthrough light also shifts the decay rate of the $D_{5/2}$ state. We add the 802 nm leakthrough desheling rate to the $D_{5/2}$ state's natural decay rate, and use this total decay rate in the maximum likelihood model. The shifts and uncertainties are given in Table I under 802 nm AOM Leak SM.

Shifts due to off-resonant optical pumping are negligible for our measurements, as detunings between transitions are at least 50 THz. We determine the off-resonant pumping rate to be less than 0.002 Hz for our laser parameters, and the maximum uncertainty due to off-resonant pumping is more than two orders of magnitude

smaller than the statistical uncertainty (See Appendix D), and thus not included in Table I.

All shifts are added linearly and uncertainties are added in quadrature for the final results in Table I. The systematic shifts and uncertainties are all smaller than the statistical uncertainties so they do not shift the statistical results significantly.

V. THEORY

We evaluated the reduced matrix elements of the electric dipole $P_{3/2} - S_{1/2}$ and $P_{3/2} - D_{3/2,5/2}$ transitions in Ra^+ using the high-precision relativistic coupled-cluster single double triple (CCSDT) method developed in [14–16]. Ra^+ was considered as a univalent ion. We constructed the basis set in V^{N-1} approximation (where N is the number of electrons) in the framework of Dirac-Fock approach, using 50 basis set B-spline orbitals of order 9 defined on a nonlinear grid with 500 points.

These MEs were calculated previously in Ref. [4] in the framework of linearized coupled-cluster single double approximation. In this work we apply more general CCSDT approach, additionally including valence triple excitations and non-linear (NL) terms into consideration. The Breit interaction and quantum electrodynamic (QED) corrections were also taken into account.

The coupled cluster equations were solved in a basis set consisting of single-particle states. In the equations for singles and doubles the sums over excited states were carried out with 45 (of 50) basis orbitals with orbital quantum number $l \leq 6$. The equations for triples were solved *iteratively* [16] but due to high computational demands we applied the following restrictions: (i) the core electrons excitations were allowed from the $[4s - 6p]$ core shells, (ii) the maximal orbital quantum number of all excited orbitals was equal to 3, and (iii) the largest principal quantum number n of the virtual orbitals where excitations were allowed was 22.

The single-electron electric dipole moment operator, \mathbf{D} , is determined as $\mathbf{D} = -|e|\mathbf{r}$, where e is the electron charge and \mathbf{r} is the radial position of the valence electron. The reduced MEs $\langle S_{1/2} || D || P_{3/2} \rangle$ and $\langle D_j || D || P_{3/2} \rangle$ (in units of $|e|a_0$, where a_0 is the Bohr radius) are presented in Table II and compared with other available data.

TABLE II. Reduced MEs $\langle S_{1/2}||D||P_{3/2}\rangle$ and $\langle D_j||D||P_{3/2}\rangle$ (in $|e|a_0$). The values obtained in the LCCSD approximation and different corrections (see the main text for more details) are presented. The final values are obtained as the sum of the LCCSD values and all corrections listed on the lines 2-5. The uncertainties of the recommended values (labeled as “Recomm.”) are given in parentheses.

	$\langle S_{1/2} D P_{3/2}\rangle$	$\langle D_{3/2} D P_{3/2}\rangle$	$\langle D_{5/2} D P_{3/2}\rangle$
LCCSD	4.511	1.512	4.823
$\Delta(\text{NL})$	0.056	0.028	0.080
$\Delta(\text{vT})$	-0.083	-0.031	-0.087
$\Delta(\text{Breit})$	0.0002	-0.002	-0.011
$\Delta(\text{QED})$	0.005	-0.002	-0.006
Final	4.489	1.505	4.799
Recomm.	4.489(22)	1.505(7)	4.799(23)
Ref. [4]	4.511	1.512	4.823
Ref. [6]	4.482	1.496	4.795
Ref. [19]	4.54(2)	1.54(2)	4.83(8)

The results given on the line labeled “LCCSD” are obtained in the LCCSD approximation. The lines 2-5 give different corrections. The corrections due to NL terms and valence triples are given on the lines 2 and 3. On the lines labeled “ $\Delta(\text{Breit})$ ” and “ $\Delta(\text{QED})$ ” we present the Breit interaction and QED corrections, respectively. Both these corrections give a small contribution. For instance, the fractional contribution of the QED correction to the $\langle S_{1/2}||D||P_{3/2}\rangle$ ME is only 0.12%, which is in a good agreement with the value 0.14% obtained in Ref. [17]. The final values are obtained as the sum of the LCCSD values and all corrections listed on the lines 2-5. We consider the final values as the recommended ones.

There are two main sources of uncertainties of the recommended values. First one is due to inaccuracy in calculation of the correlation corrections and another one is due to uncertainty of the QED corrections. The first uncertainty is estimated as the difference between the “Final” and “LCCSD” values. The uncertainty of the QED corrections are estimated to be $\sim 25\%$. However, these corrections are small and their contribution to the uncertainty budget is negligible.

We note that our results are in very good agreement with the results obtained in the framework of the LCCSD approximation used in Ref. [4]. As illustrated by Table II, the triple and NL corrections essentially cancel each other. Thus, such a good agreement is not surprising. Our results are also in a good agreement with those obtained by Roberts *et al.* [6] (where a different approach based on correlation potential method [18] was used) and with the results of Ref. [5], where a similar, relativistic coupled cluster method, was applied.

Using the MEs given in Table II we are able to find the total decay rate of the $P_{3/2}$ state, W_{tot} , and the branching ratios, r , s , and t , (determined earlier) in different approximations. The total rate can be written as the sum

TABLE III. Branching fractions r , s , t , and W_{tot} (in 10^8 s^{-1}), obtained in different approximations, are listed. The recommended values (labeled as “Recomm.”) are compared to the experimental results obtained in this work (labeled as “Experim.”) and previous theoretical results, Refs. [4, 6, 19]. The uncertainties are given in parentheses.

	r	s	t	W_{tot}
LCCSD	0.8768	0.1078	0.01541	2.116
CCSD	0.8758	0.1086	0.01558	2.172
LCCSDT	0.8768	0.1079	0.01534	2.049
CCSDT	0.8757	0.1087	0.01553	2.093
Final	0.8768	0.1078	0.01543	2.096
Recomm.	0.8768(11)	0.1078(9)	0.01543(17)	2.096(18)
Experim.	0.87678(20)	0.10759(10)	0.01563(21)	
Ref. [6]	0.8767	0.1080	0.0153	2.089
Ref. [4]	0.8767	0.1078	0.0154	2.117
Ref. [19]	0.8773	0.1069	0.0158	2.142(42)

of the $P_{3/2} - S_{1/2}$ and $P_{3/2} - D_{5/2,3/2}$ transition rates, $W_{\text{tot}} = W_r + W_s + W_t$, where $W_r \equiv W(P_{3/2} \rightarrow S_{1/2})$, $W_s \equiv W(P_{3/2} \rightarrow D_{5/2})$, and $W_t \equiv W(P_{3/2} \rightarrow D_{3/2})$. The probability of the $M1 P_{3/2} - P_{1/2}$ transition is negligibly small compared to the transition rates of other decay channels.

The results obtained in different approximations are given in the respective rows in Table III. The CCSD results include NL terms but not triples, LCCSDT results include triples but not NL terms, and CCSDT values include both the NL terms and triples. “Final” results for r , s , t , and W_{tot} are obtained as the sum of the “CCSDT” values and the Breit interaction and QED corrections.

The absolute uncertainty, ΔW_{tot} , of the total decay rate of the $P_{3/2}$ state is determined as

$$\Delta W_{\text{tot}} = \sqrt{(\Delta W_s)^2 + (\Delta W_r)^2 + (\Delta W_t)^2}, \quad (4)$$

where the absolute uncertainties ΔW_s , ΔW_r , and ΔW_t are found using the uncertainties of the respective MEs given in Table II. For calculation of the transition rates we use the experimental energies [20] that are known with a high accuracy and do not contribute to the uncertainty budget.

Using the calculated MEs, we found the total decay rate of the $P_{3/2}$ state and the branching fractions. The uncertainties of the branching fractions, r , s , and t , are estimated as the largest differences between the “LCCSD” results and the results obtained in the listed approximations. If the lifetime of the $P_{3/2}$ state is measured with a high precision, then using the experimental values for branching fractions we will be able to extract the values of the electric dipole MEs of the $P_{3/2} - S_{1/2}$ and $P_{3/2} - D_{3/2,5/2}$ transitions with a high accuracy.

There is very good agreement between the theoretical and experimental results. Using the MEs given in Refs. [6, 19] we have calculated r , s , t , and W_{tot} . These

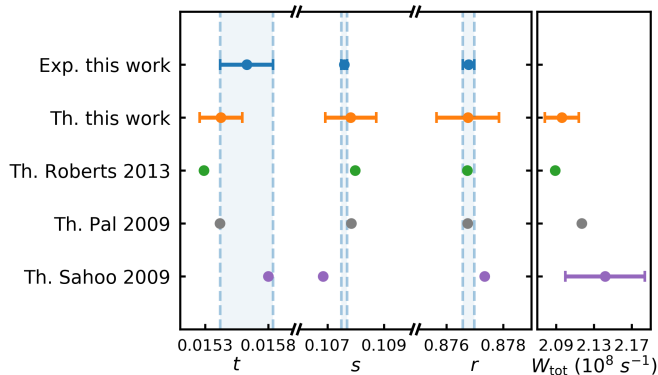


FIG. 4. Comparison of the experimental results on branching fractions r , s , and t and theoretical calculations from this work, Th. Roberts 2013 [6], Th. Pal 2009 [4], and Th. Sahoo 2009 [19]. Theoretically calculated values of the $P_{3/2}$ state total decay rates are shown.

results, also presented in Table III for comparison, are in agreement with our values.

Using the recommended values of s and t and applying the same approach for estimating uncertainty we find the ratio $s/t = 6.990(43)$. This value is in a good agreement with the experimental result $s/t = 6.884(92)$ but is two times more accurate. Given the theoretical ratio of s/t and the experimental high-accuracy value of $s = 0.10759(10)$ we can extract the value $t = 0.01539(10)$.

VI. SUMMARY

Good agreement is found between measurements of the radium ion's $P_{3/2}$ branching fractions and new theoretical values, as well as with previous theoretical works, see

$$D(N; N_d, N_b) = (1 - t_0 p_{\text{decay}})P(N; N_d) + \int_0^{t_0} p_{\text{decay}} P(N; (N_b - N_d)(1 - t/t_0) + N_d) dt \quad (\text{A1})$$

where $P(N; N_0)$ is the probability that a Poisson distribution with average value N_0 yields N , and $p_{\text{decay}} = (\tau_{5/2})^{-1}$ is the $D_{5/2}$ state's decay rate. The probability mass function for bright PMT counts is given by the Poisson distribution $B(N; N_b) = P(N; N_b)$. We model the combined probability mass function for all PMT counts as

$$E(N; N_d, N_b, p_d) = p_d D(N; N_d, N_b) + p_b B(N; N_b) \quad (\text{A2})$$

where p_d is the state measurement probability for dark events, and for bright events $p_b = 1 - p_d$.

We use a maximum likelihood method to determine p_d with Eq. A2. To do this we maximize $\prod_i p_i$ by varying

Fig. 4. The measurement precision of the $P_{3/2}$ branching fraction to the $S_{1/2}$ state supports a 0.1% calculation of the $\langle S_{1/2} || D || P_{3/2} \rangle \langle D_{3/2} | H_{\text{PNC}} | P_{3/2} \rangle$ PNC amplitude term, where H_{PNC} is the PNC Hamiltonian that mixes opposite parity states with the same total electronic angular momentum. This term accounts for $\sim 6\%$ of the total PNC amplitude in a Ra^+ $S_{1/2} - D_{3/2}$ PNC experiment [4]. The measured $P_{3/2}$ branching fractions in this work can be combined with Ra^+ light shift measurements to determine the $\langle D_{3/2} || D || P_{1/2} \rangle$ matrix element [19], this will improve the precision of the largest PNC contribution, the $\langle D_{3/2} || D || P_{1/2} \rangle \langle S_{1/2} | H_{\text{PNC}} | P_{1/2} \rangle$ term [4].

This research was performed in part under the sponsorship of the Office of Naval Research, Grant No. N00014-17-1-2252, NSF Grants No. PHY-1912665 and PHY-1620687, and the UC Office of the President (MRP-19-601445). S.P. acknowledges support by Russian Science Foundation under grant No. 14-31-00022.

Appendix A: State measurement

The 468 nm fluorescence during state measurement is uniformly distributed. An ion that decays during state measurement from the $D_{5/2}$ state results in $(N_b - N_d)(1 - t/t_0) + N_d$ PMT counts on average, where t_0 is the state measurement time, t is the time of decay, N_b (N_d) is the average number of PMT counts for bright (dark) events. Because the state measurement time is much shorter than the $D_{5/2}$ state lifetime, $\tau_{5/2}$, we approximate the decay probability during state measurement as a constant, and therefore the total decay probability during state measurement is $t_0/\tau_{5/2}$. The probability mass function of PMT dark event counts considering $D_{5/2}$ decays during state measurement is

N_d , N_b , and p_d , where $p_i = E(N_i; N_d, N_b, p_d)$ where N_i are the PMT counts for the i -th state measurement. The parameters that maximize $\prod_i p_i$ are the maximum likelihood results.

With p_d and the total number of measurements, M , the dark state probability uncertainty is $\Delta p_d = \sqrt{p_d(1 - p_d)/M}$ [10].

Appendix B: Collisional and motional heating rate

We measure the combined collision and motional heating rate using a pulse sequence that does 1 ms state detection (which cools the ion) after 10 ms of dark time. If

TABLE IV. Maximum off-resonant pumping rate of all relevant dipole transitions by lasers used in the experiment.

Light wavelength	$S_{1/2} - P_{3/2}$	$S_{1/2} - P_{1/2}$	$D_{3/2} - P_{3/2}$	$D_{5/2} - P_{3/2}$	$D_{3/2} - P_{1/2}$
422 nm	8×10^{-7} Hz	...	1×10^{-4} Hz	2×10^{-5} Hz	8×10^{-6} Hz
708 nm	1×10^{-7} Hz	2×10^{-7} Hz	...	5×10^{-4} Hz	5×10^{-5} Hz
802 nm	1×10^{-7} Hz	1×10^{-7} Hz	2×10^{-3} Hz	...	1×10^{-4} Hz
1079 nm	6×10^{-8} Hz	7×10^{-8} Hz	3×10^{-4} Hz	1×10^{-4} Hz	...

a dark event is detected either a collision or heating event occurred. During 13500 s of measurement, we detected 23 dark events (consecutive dark events are counted as a single event, as the ion was either shelved in the $D_{5/2}$ state due to an inelastic collision, or still hot due to a collision or motional heating). This gives a combined collision and motional heating rate of 0.0017(4) Hz.

Appendix C: AOM leakthrough deshelving rates

468 nm: The 468 nm AOM leakthrough deshelving rate is measured using a pulse sequence that initializes the ion in the $S_{1/2}$ state, and then waits 50 ms before a 50 μ s long 708 nm pulse. The 50 ms wait time is short compared to the calculated $D_{3/2}$ lifetime, 638(10) ms [4], so if population was shelved by 468 nm AOM leakthrough light, the ion is most likely in the $D_{3/2}$ state at the end of the wait time. Light at 708 nm pumps 11% of any population from the $D_{3/2}$ to $D_{5/2}$ (from the $P_{3/2}$ branching fractions measured in this work). After the 708 nm pulse, we state detect for 1 ms to measure the the $D_{5/2}$ population. The measured deshelving rate from the $S_{1/2}$ state to the $D_{3/2}$ state by 468 nm leakthrough light is 0.0045(10) Hz.

708 nm: We measure the 708 nm AOM leakthrough by initializing the population in the $D_{3/2}$ state and measuring the population in the $D_{5/2}$ state after a 2 ms delay with state detection. The measured $D_{3/2}$ state deshelving rate due to 708 nm AOM leakthrough light is 0.005(2) Hz. Because the delay time is short compared to the lifetimes of the $D_{5/2}$ and $D_{3/2}$ states [4], the shift due to either $D_{5/2}$ or $D_{3/2}$ decays during the 2 ms delay is negligible compared to the statistical uncertainty.

802 nm: We initialize the ion in the $D_{5/2}$ state,

and measure its population after a 300 ms wait time first with the 802 nm light blocked by a mechanical shutter and second without the 802 nm shutter. Both data sets are fitted to exponential decays. With the shutter the decay rate is 3.29(10) Hz and without the shutter the rate is 3.69(14) Hz. This gives a $D_{5/2}$ deshelving rate of 0.40(17) Hz due to 802 nm AOM leakthrough.

1079 nm: Measuring the 1079 nm AOM leakthrough is complicated by decays of the $D_{3/2}$ state. We initialize population in the $D_{3/2}$ state and then wait 100 ms before pumping a fraction of the population to the $D_{5/2}$ state through the $P_{3/2}$ state. By measuring the $D_{5/2}$ population we can infer the $D_{3/2}$ population at the end of the wait time. Deshelving due to 708 nm and 1079 nm AOM leakthrough, as well as spontaneous decays results in a total decay rate of 1.90(20) Hz. This decay rate is greater than the spontaneous decay rate of 1.57(2) Hz due to the theoretical natural lifetime [4]. With the measured 708 nm deshelving rate and the spontaneous decay rate, the 1079 nm AOM leakthrough deshelving rate is 0.33(20) Hz.

Appendix D: Off-resonant pumping

We analyzed the systematic effects due to off-resonant optical pumping. Table IV summarizes the off-resonant pumping rates for all relevant dipole transitions assuming maximum light intensity at the ion (*i.e.* we assume the ion is centered in a Gaussian beam). If we assume that all off-resonant pumping shifts the branching fraction values in the same direction we find that the shift is 2 orders of magnitude smaller than the statistical uncertainty. Therefore we do not include off-resonant pumping as a systematic uncertainty in Table I.

[1] N. Fortson, Phys. Rev. Lett. **70**, 2383 (1993).
[2] M.-A. Bouchiat and C. Bouchiat, Rep. Prog. Phys. **60**, 1351 (1997).
[3] K. P. Geetha, A. D. Singh, B. P. Das, and C. S. Unnikrishnan, Phys. Rev. A **58**, R16 (1998).
[4] R. Pal, D. Jiang, M. S. Safronova, and U. I. Safronova, Phys. Rev. A **79**, 062505 (2009).
[5] B. K. Sahoo, B. P. Das, R. K. Chaudhuri, D. Mukherjee, R. G. E. Timmermans, and K. Jungmann, Phys. Rev. A **76**, 040504 (2007).

[6] B. M. Roberts, V. A. Dzuba, and V. V. Flambaum, Phys. Rev. A **88**, 012510 (2013).
[7] S. G. Porsev, K. Beloy, and A. Derevianko, Phys. Rev. D **82**, 036008 (2010).
[8] S. G. Porsev, M. S. Safronova, U. I. Safronova, V. A. Dzuba, and V. V. Flambaum, Phys. Rev. A **98**, 052512 (2018).
[9] M. Fan, C. A. Holliman, A. L. Wang, and A. M. Jayich, Phys. Rev. Lett. **122**, 223001 (2019).
[10] R. Gerritsma, G. Kirchmair, F. Zähringer, J. Benhelm, R. Blatt, and C. F. Roos, Eur. Phys. J. D **50**, 13 (2008).

- [11] H. Zhang, M. Gutierrez, G. H. Low, R. Rines, J. Stuart, T. Wu, and I. Chuang, *New J. Phys.* **18**, 123021 (2016).
- [12] T. Dutta, D. De Munshi, D. Yum, R. Rebhi, and M. Mukherjee, *Scientific Reports* **6**, 29772 (2016).
- [13] T. Pruttivarasin and H. Katori, *Rev. Sci. Instrum.* **86**, 115106 (2015).
- [14] S. A. Blundell, W. R. Johnson, Z. W. Liu, and J. Sapirstein, *Phys. Rev. A* **40**, 2233 (1989).
- [15] S. A. Blundell, W. R. Johnson, and J. Sapirstein, *Phys. Rev. A* **43**, 3407 (1991).
- [16] S. G. Porsev and A. Derevianko, *Phys. Rev. A* **73**, 012501 (2006).
- [17] B. M. Roberts, V. A. Dzuba, and V. V. Flambaum, *Phys. Rev. A* **87**, 054502 (2013).
- [18] V. A. Dzuba, V. V. Flambaum, P. G. Silvestrov, and O. P. Sushkov, *J. Phys. B* **20**, 1399 (1987).
- [19] B. K. Sahoo, L. W. Wansbeek, K. Jungmann, and R. G. E. Timmermans, *Phys. Rev. A* **79**, 052512 (2009).
- [20] Yu. Ralchenko, A. Kramida, J. Reader, and the NIST ASD Team (2011). NIST Atomic Spectra Database (version 4.1). Available at <http://physics.nist.gov/asd>. National Institute of Standards and Technology, Gaithersburg, MD.